

# A Zero-Gap Gas Phase Photoelectrolyzer for CO<sub>2</sub> Reduction with Porous Carbon Supported Photocathodes

Yujie Zhao,<sup>[a]</sup> Ivan Merino-Garcia,<sup>[b]</sup> Jonathan Albo,<sup>[b]</sup> and Andreas Kaiser<sup>\*[a]</sup>

A modified Metal-Organic Framework UiO-66-NH<sub>2</sub>-based photocathode in a zero-gap gas phase photoelectrolyzer was applied for CO<sub>2</sub> reduction. Four types of porous carbon fiber layers with different wettability were employed to tailor the local environment of the cathodic surface reactions, optimizing activity and selectivity towards formate, methanol, and ethanol. Results are explained by mass transport through the different type and arrangement of carbon fiber support layers in the photo-

cathodes and the resulting local environment at the UiO-66-NH<sub>2</sub> catalyst. The highest energy-to-fuel conversion efficiency of 1.06% towards hydrocarbons was achieved with the most hydrophobic carbon fiber (H23C2). The results are a step further in understanding how the design and composition of the photoelectrodes in photoelectrochemical electrolyzers can impact the CO<sub>2</sub> reduction efficiency and selectivity.

## Introduction

Large quantities of CO<sub>2</sub> are released into the atmosphere every year, reaching a total of 37.4 Gt per year.<sup>[1]</sup> Electrocatalytic (EC) and photo-electrocatalytic (PEC) CO<sub>2</sub> reduction are sustainable technologies that can directly convert CO<sub>2</sub> with surplus electricity into valuable chemicals and fuels.<sup>[2]</sup> In the PEC process, sunlight can be utilized in addition to electricity by using photoelectrodes and the photogenerated electrons can be efficiently separated during the CO<sub>2</sub> reduction in contrast to simple photocatalysis (PC).<sup>[3]</sup> However, PEC is a complex process that can result in a variety of products depending on several factors including: i) the exact configuration of the PEC cell<sup>[4]</sup>, ii) the reaction and transport medium for CO<sub>2</sub> (and other reactants), and iii) the choice of materials and their structuring into a photocathode.

Most studied PEC systems for CO<sub>2</sub> reduction use a liquid electrolyte as reaction medium with ionic exchange membranes,<sup>[5]</sup> most commonly a buffered aqueous bicarbonate solution.<sup>[6]</sup> In an alternative configuration, the CO<sub>2</sub> can be directly converted from the gas phase in an advanced electrolyzer, by using gas-fed systems with a zero-gap gas diffusion electrode (GDE) as part of a membrane electrode assembly (MEA).<sup>[7]</sup> This zero-gap gas phase PEC configuration could

increase the conversion efficiency because of i) efficient gas distribution, ii) removal of products over the cell,<sup>[8]</sup> iii) improved charge separation by additional bias<sup>[9]</sup>, and iv) photoelectric synergistic catalysis<sup>[10]</sup> with enhanced activity and selectivity of semiconductor catalysts towards CO<sub>2</sub> reduction. Moreover, traditional electrolysis systems often suffer from energy losses due to overpotential, resistance, and other inefficiencies. However, in zero-gap gas phase systems, by eliminating the need for a liquid electrolyte and minimizing the distance between the electrodes, these energy losses can be minimized, leading to an improved overall efficiency. Nevertheless, specific studies on gas phase reduction of CO<sub>2</sub> in zero-gap PEC configurations are very scarce. Additional information and relevant principles could instead be obtained from studies on EC systems with aqueous electrolytes and then applied to gas phase PEC systems. In general, the performance of a GDE<sup>[11]</sup> at the triple phase boundaries depends on mass transfer, availability and surface coverage of core reactants, such as CO<sub>2</sub> and protons, and the formed products, all determining the overall surface reaction kinetics and formation of products. Beneath the CO<sub>2</sub>, water and hydrated cations are involved in these elementary processes in the CO<sub>2</sub>RR.<sup>[12]</sup> Thus, an appropriately designed GDE that takes advantage of the differential transport characteristics of each reaction should, in principle, enable enhanced selectivity towards specific products.<sup>[13]</sup> The selectivity towards specific products should not only depend on the mass transfer kinetics<sup>[14]</sup> but also on the thermodynamically elementary rate-determining steps on the photocatalyst material, considering that the CO<sub>2</sub> reduction also involves the process of multielectron transfer accompanied by multiphoton coupling in a PEC system.

Moreover, metal organic frameworks (MOFs) with ultrahigh surface area, and tailored pore size and chemistry were explored as catalysts to optimize the triple phase boundaries. Mechanistically, unsaturated metal coordination sites in MOFs have shown to enhance the CO<sub>2</sub> reduction towards hydrocarbons<sup>[15]</sup> and by defect engineering of MOFs open sites can be created that allow stronger interaction with the CO<sub>2</sub>

[a] Dr. Y. Zhao, Assoc. Prof. Dr. A. Kaiser  
Department of Energy Conversion and Storage  
Technical University of Denmark  
2800, Kgs. Lyngby, Denmark  
E-mail: akai@dtu.dk

[b] Dr. I. Merino-Garcia, Assoc. Prof. Dr. J. Albo  
Departamento de Ingenierías Químicas y Biomoleculares  
Universidad de Cantabria  
Avda. Los Castros s/n. 39005 Santander, Spain

Supporting information for this article is available on the WWW under <https://doi.org/10.1002/cssc.202400518>

© 2024 The Authors. ChemSusChem published by Wiley-VCH GmbH. This is an open access article under the terms of the Creative Commons Attribution License, which permits use, distribution and reproduction in any medium, provided the original work is properly cited.

molecule.<sup>[16]</sup> For, example, amino functionalized UiO-66 (UiO-66-NH<sub>2</sub>) has been examined for photocatalytic CO<sub>2</sub> reduction. In this case, the amino functional groups acted as electron donors for photogenerated electrons<sup>[17]</sup>, CO,<sup>[18]</sup> methanol<sup>[19]</sup> and CH<sub>4</sub>.<sup>[20]</sup> have been observed as reaction products. Nevertheless, the overall performance of the UiO-66-NH<sub>2</sub> photocatalyst was limited by high resistance due to insufficient charge transfer. In principle, charge separation efficiency in UiO-66-NH<sub>2</sub> could be improved by using this material as a photocathode in a PEC system.

In this study, we investigate the influence of different carbon support layers and photocathode configurations in a zero-gap gas phase PEC electrolyzer based on a proton exchange membrane (PEM) on the CO<sub>2</sub>RR performance under visible light irradiation. Defective UiO-66-NH<sub>2</sub> was selected and assembled in different carbon support layers based on commercial and self-made carbon fiber mats, following procedures to fabricate MOF nanofiber architectures.<sup>[21]</sup> The results were interpreted with respect to the diffusion of the reactants (CO<sub>2</sub>, H<sub>2</sub>O and protons) and the transportation of cations (K<sup>+</sup>).

## Results and Discussion

### Physicochemical Properties

Scanning Electron Microscopy (SEM) shows the defective UiO-66-NH<sub>2</sub> MOF photocatalyst that was synthesized, and spray coated on commercial carbon fiber mats or prepared by in-situ growth on carbon nanofibers (Figure S1a and S1b). The materials, carbon layers, and preparation as photocathodes for the different photocatalysts with hydrophilic and hydrophobic properties are summarized in Table S1. The UiO-66-NH<sub>2</sub> raw powder consisted of sub-micron sized crystallites of about 75 nm (Figure S1a). The hydrophilic carbon nanofibers, prepared by electrospinning and carbonization, had a diameter of about 375 nm and fiber mat thickness of 180 μm (Figure S2a–c).

Results from Raman spectra show typically D and G peaks (Figure S2d), indicating the transformation of the PAN polymer nanofibers into a CNF with conductive graphite structure during carbonization. The microstructure of well-distributed nanocrystalline UiO-66-NH<sub>2</sub> particles on the CNF surface can be observed by SEM and EDX (Figure S3) with a uniform crystallite size of about 75 nm. The corresponding distribution of element ratios is summarized in Table S2. So called 'Reo defects' in MOF have been reported before and were observed in the XRD patterns (Figures S1c and d) of UiO-66-NH<sub>2</sub>, implying missing cluster defects and enlarged pores in the framework.<sup>[16a,b]</sup> FTIR spectra (Figure S4a) further demonstrate the defective structure of this Zr-based MOF with amino functional groups and F containing groups.<sup>[22]</sup> The band at 1203 cm<sup>-1</sup> is attributed to -CF<sub>3</sub> from TFA modulators, indicating the missing clusters defects due to the capping effect of TFA.<sup>[23]</sup> Comparing the TGA results of UiO-66, the defective UiO-66-NH<sub>2</sub> and "ideal" Zr<sub>6</sub>O<sub>6</sub>(BDC-NH<sub>2</sub>)<sub>6</sub> further confirm the presence of missing cluster defects (Figure S4b) because the normalized weight for the defective UiO-66-NH<sub>2</sub> is higher than the theoretical value of 232% of Zr<sub>6</sub>O<sub>6</sub>(BDC-NH<sub>2</sub>)<sub>6</sub>.<sup>[24]</sup>

The loading of UiO-66-NH<sub>2</sub> on the MOF-CNF composite was calculated with 11.6 wt% based on the TGA results (Figure S4c).

UiO-66-NH<sub>2</sub> and CNF@UiO-66-NH<sub>2</sub> exhibit higher selectivity of CO<sub>2</sub> adsorption because of the amine functional group and unsaturated Zr sites. The higher specific surface area and fine distribution of UiO-66-NH<sub>2</sub> are also responsible for the high CO<sub>2</sub> uptake (as shown in Figure 1a). UiO-66-NH<sub>2</sub> exhibits higher BET surface area (1024 m<sup>2</sup>g<sup>-1</sup>) and pore volume (0.65 cm<sup>3</sup>g<sup>-1</sup>) as can be seen in Figure S5 and Table S3. The pore size distributions obtained by the non-local density functional theory (NLDFT) in Figure S5 further demonstrate the presence of mesopores in UiO-66-NH<sub>2</sub>. A pore width of 1.1–1.9 nm can be attributed to 'Reo defects,' which is in line with the XRD results. Notably, as described by previous research, the missing linker defects cannot form mesopores.<sup>[25]</sup> Hence, the mesopores included in the synthesized UiO-66-NH<sub>2</sub> are due to missing clusters, resulting in higher amounts of coordinatively unsaturated Zr atoms. UV-vis spectroscopy on UiO-66-NH<sub>2</sub> (Figure 1b) revealed an additional light absorption band for the defective UiO-66-NH<sub>2</sub> at 380 nm, which can be attributed to a "linker to cluster" charge transfer (LCCT), suggesting extended light absorption in the visible light region and charge transfer by LCCT for the defective UiO-66-NH<sub>2</sub> material used in these studies.<sup>[26]</sup>

### Photoelectrochemical Properties

The on-off performance of photocathodes with hydrophilic carbon layers has been analysed as a function of applied potential by cyclic voltammetry for the competing CO<sub>2</sub>RR and hydrogen evolution reaction (HER) in gas phase CO<sub>2</sub> reduction, using the UiO-66-NH<sub>2</sub>-based photocathodes (Figure 2).

For the hydrophilic CNF and superhydrophilic H23 carbon layers, the hysteresis in the CVs between -1 V and 0.5 V indicates the formation of an electrical double layer caused by the diffusion of H<sub>2</sub>O and ions onto the surface of the photocathode. The current densities and hysteresis in the CV are larger for the CNF compared to the H23 photocathodes because of the larger surface area of the nanofibers compared to the microfibers in the H23. These results reveal that the catalysts and the carbon layers were thoroughly wetted by H<sub>2</sub>O in the hydrophilic carbon layers, which results in increasing HER while the diffusion of CO<sub>2</sub> to the active sites and thereby CO<sub>2</sub>RR is limited. Under light irradiation, the current density of H23-

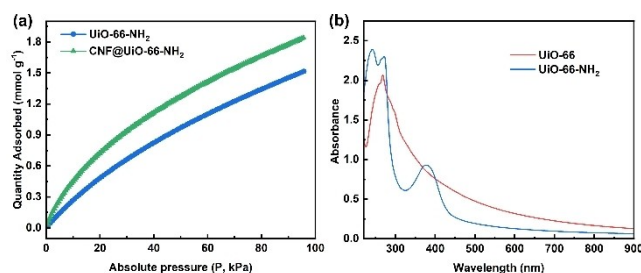


**Figure 1.** CO<sub>2</sub> uptake at 298 K (a) and light absorption spectra (b) of UiO-66-NH<sub>2</sub> and CNF@UiO-66-NH<sub>2</sub>, respectively.

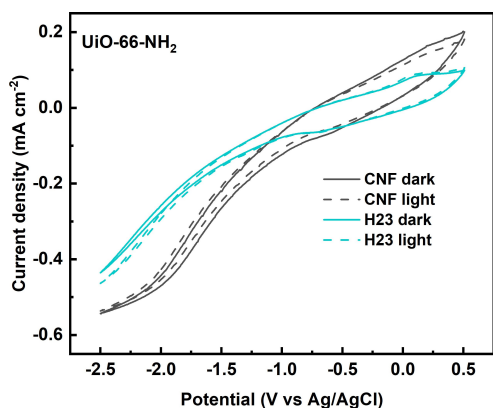
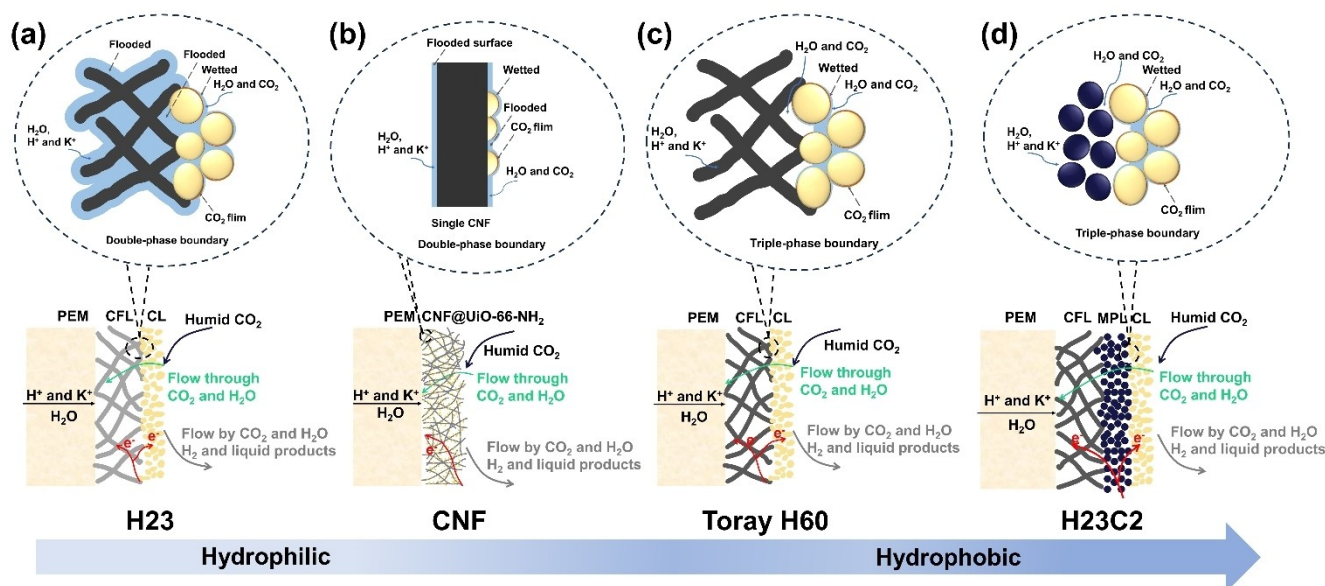


**Figure 2.** On-off cyclic voltammetry (CV) curves at  $50 \text{ mVs}^{-1}$  of UiO-66-NH<sub>2</sub> with hydrophilic carbon support layers in PEC configuration under dark and light irradiation.

based photocathodes increased while that of CNF based photocathodes slightly decreased. This can be explained by the different configuration of these photocathodes (Scheme 1a compared to 1b), in which the photocatalyst located in the top CL of the H23 carbon layer is more directly exposed to the light compared to the catalysts in the CNF layer that absorbs more than 90% light due to the black color and the intrinsic, fine three-dimensional nanostructure.<sup>[27]</sup> Hence, the CNF based photocathode does even show a slight negative light response. Moreover, the polarization of the CNF-based photocathode is stronger, suggesting a higher concentration of ions and liquid 'products', which could lead to lower catalytic performance because of the degradation of the MOF catalysts.<sup>[28]</sup> Degrada-

tion of the UiO-66-NH<sub>2</sub> MOF will be discussed in more detail further below.

The CVs of the hydrophobic photocathodes (Toray H60 and H23C2) reach approximately similar current densities without illumination (Figure 3, referring to same photocathode configuration as shown in Scheme 1c and d). Interestingly, the electrodes with the superhydrophobic H23C2 substrates show more positive onset potential compared to the electrodes with Toray H60, which could be explained by an improved interface between the catalysts and the carbon layer by the additional microporous layer (MPL). Except for the CV curves of the Toray H60 based photocathode, the other CV curves of all photocathodes (including the hydrophilic photocathodes) exhibit polarization at lower potential, suggesting stronger accumulation of reaction products and ions on the electrode surfaces. For the Toray H60 based photocathode, the current density slightly increased under visible light irradiation (dashed CV curve in Figure 3). The HER is favored by using the less hydrophobic Toray H60 carbon layer at (more) negative potentials. In addition, the polarization of this type of electrode is weaker than H23C2-based photocathodes, implying higher electrochemical dynamic reaction kinetics due to less exposed active sites. In contrast to this, the polarization of the H23C2 based photocathode is stronger, suggesting a higher concentration of ions and liquid products. Looking at the light illumination on the different photocathode configurations in PEC operation (Scheme 1), only for those electrodes that do show less polarization (i.e. the Toray H60 based electrodes), the light positively affects the activity of the catalysts. Those electrodes that show stronger polarization (e.g., H23C2), do not have an apparent 'light response'.



**Scheme 1.** Schematic of different photocathode configurations and interfaces between carbon layers and catalysts based on different types of carbon layers for gas phase CO<sub>2</sub>RR, investigated in a zero-gap electrolyzer. The CO<sub>2</sub> and H<sub>2</sub>O transport pathways in the electrodes are indicated here for different photocathodes in PEC configuration. The carbon support layer could be an individual carbon fiber layer (CFL), a carbon nanofiber layer (CNF) or multilayer with both a CFL and microporous carbon layer (MPL). Further layers are a catalysts layer (CL) and a proton exchange membrane (PEM) of Nafion®117.

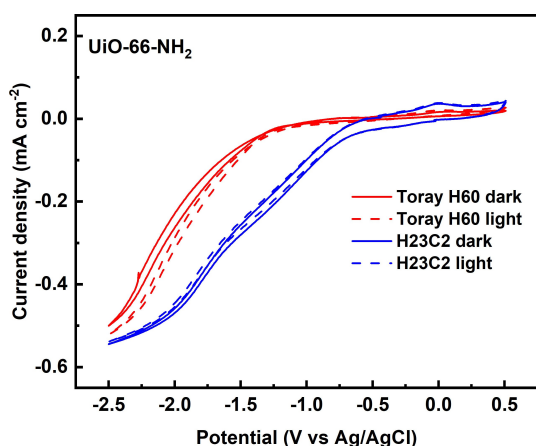


**Figure 3.** On-off CV curves at  $50 \text{ mV s}^{-1}$  of UiO-66-NH<sub>2</sub> with hydrophobic carbon support layers in EC configuration and PEC configuration under dark and light irradiation.

### CO<sub>2</sub>RR Performance in Zero-gap Photoelectrolyzers

The selectivity for the formation of products on the UiO-66-NH<sub>2</sub> based photocathodes in the different types of carbon support layer assemblies has been evaluated by continuous CO<sub>2</sub> reduction tests in the photoelectrolyzer. Chronopotentiometry was used to measure the CO<sub>2</sub>RR performance of the photocathodes in the PEC system at  $-7.5 \text{ mA cm}^{-2}$  for an hour. Figure 4 reveals that in "light" and "dark" mode the product selectivity is strongly dependent on i) the wettability of the different carbon layers in the humid CO<sub>2</sub> atmosphere and ii) the configuration of the photocathodes (as schematically visualized in Scheme 1), both playing an important role in the diffusion of reactants, the reaction pathways, CO<sub>2</sub>RR vs HER, and the product distribution of CO<sub>2</sub>RR. More specifically, Figure 4 shows that the CO<sub>2</sub> reduction products of the photocathodes with different types of carbon layers in the zero-gap gas phase photoelectrolyzer under dark and light irradiation are formate,

methanol, and ethanol. Obviously, the wetting of the photocathode with water from the humid CO<sub>2</sub> gas supply depends on the type of carbon layer that was used, according to Scheme 1. Additionally, Figure S6a reveals that the production of all reaction products (H<sub>2</sub> and hydrocarbons) decreases if the carbon layer is more hydrophobic, implying the activation of carbon layer also plays a role on the activity (especially for HER). The tendency is independently on the operation mode of the electrolyzer (dark or light). Furthermore, the relative ratio of the production rates for CO<sub>2</sub>RR products (formate, methanol and ethanol) over hydrogen formation (in HER) increases for the hydrophobic carbon layers (Toray H60 and H23C2) based photocathodes. The highest hydrogen production rate observed for the superhydrophilic carbon layer (H23) can be explained by an increased wetting of the photocatalyst surface within the photocathodes and the activation of the carbon surface, which might finally lead to water flooding. The tendency for flooding of pores in the different carbon layers can be estimated by the water retention on the electrodes via Eq. S3 and S4. In general, the availability of water (or flooding) should favor the HER over CO<sub>2</sub>RR. However, reducing the wetting by employing hydrophobic GDEs as photocathodes (instead of the hydrophilic photocathodes) increases the production rates of CO<sub>2</sub>RR products relative to the HER (Figure S6a and S7a), suggesting a shift of selectivity towards CO<sub>2</sub>RR.

For a more detailed explanation of the results, the interface between the carbon layers and photocatalysts in Scheme 1 summarize schematically the pathways of CO<sub>2</sub> and H<sub>2</sub>O transport, as well as the transport of ions (i.e. H<sup>+</sup> and K<sup>+</sup>) close to the photocatalyst surface. Additionally, it also gives the corresponding visualization on the photocathode level. In all photocathodes, CO<sub>2</sub> diffusion and transport involve the flow-by and flow-through mode. Protons, potassium ions and water can be supplied by the PEM membrane to the photocatalyst in the CL (flow through mode) or by the supply of humid CO<sub>2</sub> gas (flow by mode). Proton and cation transportation pathways

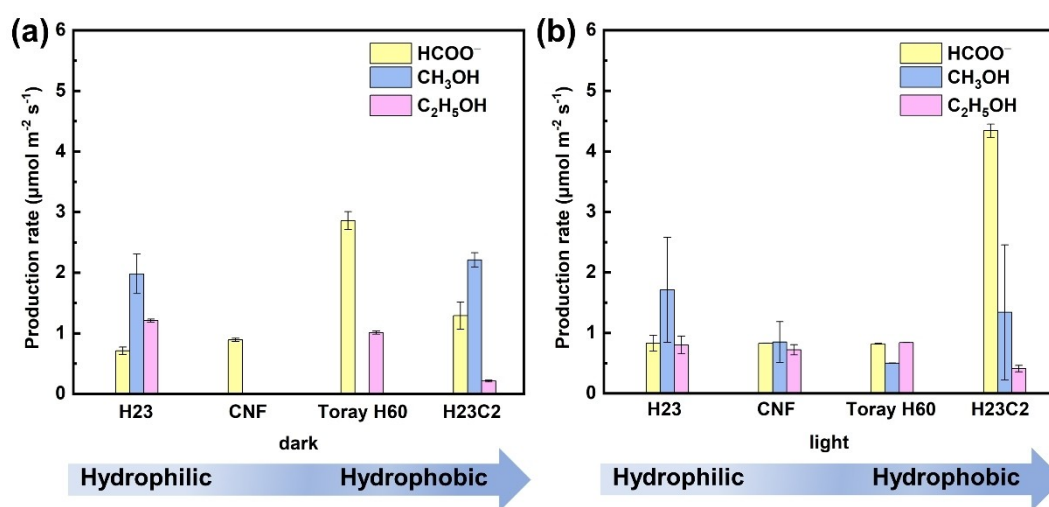


**Figure 4.** Production rates of CO<sub>2</sub>RR based on different types of carbon support layers in PEC configuration under dark (a) and light irradiation (b), respectively. The products were collected and analysed during the chronopotentiometry measurement at  $-7.5 \text{ mA cm}^{-2}$  for 1 h.

involve the migration from anolyte through the PEM.<sup>[29]</sup> Depending on the hydrophilicity of the carbon layers, water can then accumulate (condense) in the pores of the CL and form a liquid film on the photocatalysts, resulting in a new pathway for ionic transport in the carbon layer. For H<sub>2</sub>O, diffusion includes pathways from the inlet and from the anolyte via the PEM, driven by the concentration gradient.<sup>[14e]</sup> The inlet H<sub>2</sub>O acts as a proton source for CO<sub>2</sub>RR and the resulting formation of hydroxyl (OH<sup>-</sup>) ions influences the concentration of CO<sub>2</sub> in the water film, thus affecting the selectivity towards CO<sub>2</sub>RR in Toray H60 and H23C2 based photocathodes. Notably, for every electron that is consumed in CO<sub>2</sub>RR (or HER), OH<sup>-</sup> ions are produced that promote the formation of bicarbonate ions by the reaction of CO<sub>2</sub> with the water, thereby leading to a high CO<sub>2</sub> concentration on the wetted surfaces of the photocatalysts in the hydrophilic CL. The bicarbonate serves as a buffer to maintain the triple phase boundaries for CO<sub>2</sub>RR by ensuring the stability of the MOF based photocatalysts, for example in the H23 and Toray based photocathodes. The impact of the environment (alkalinity due to the formation of bicarbonate) on the stability of the UiO-66-NH<sub>2</sub> catalyst surface is discussed further below.

The special assembly of the hydrophilic CNF based photocathode (Scheme 1b) explains why only formate is formed. In this case, the catalyst is more easily wetted because it is very well-distributed onto the entire surface of a hydrophilic carbon nanofiber layer with ultrahigh surface area and pore size that led to strong capillary forces. These results align with prior studies indicating a correlation between the distribution of reaction products and the wettability of catalyst, with hydrophilic catalyst surfaces favoring formate and hydrogen production,<sup>[30]</sup> and more positive electrode potential, as shown in Figure S6.

Under light irradiation, the processes are still determined by the chemistry (wettability) and configuration of the photocatalyst in the photocathode. Figure 4b indicates that the photoexcited electrons in the MOFs could further reduce H<sub>2</sub>O and CO<sub>2</sub> within a localized environment. Thus, the PEC process has the potential to modulate the activity and selectivity towards HER and CO<sub>2</sub>RR. The H23 based photocathodes increase activity and selectivity towards the HER (Figure S6b and S7). This enhancement is attributed to the fully wetted surface of the hydrophilic electrode, leading to the accumulation of OH<sup>-</sup> and HCO<sub>3</sub><sup>-</sup>. Interestingly, alcohols are observed on the CNF based photocathodes in Figure 4b, suggesting a photothermal effect<sup>[31]</sup> on the product distribution. It is in line with prior studies that the reaction temperature has an effect on the product distribution and selectivity of the CO<sub>2</sub>RR process due to the different thermodynamic behavior of CO<sub>2</sub>RR and HER.<sup>[32]</sup>

The H<sub>2</sub>O from the humid CO<sub>2</sub> gas stream would diffuse and accumulate in the pores of the hydrophilic CL over time. This would lead to the formation of a continuous liquid film on the hydrophobic carbon layers and flooded surface on the photocatalyst surface for the hydrophilic photocathodes, thereby creating a new pathway for ionic transport and leading to more positive electrode potentials, as shown in Figure S8.

The initial potential of hydrophilic photocathodes are high, suggesting a high resistance due to ohmic resistance of the PEM and the photocathodes in Figure S8a. However, due to up-concentration of K<sup>+</sup>, H<sub>2</sub>O, and CO<sub>2</sub> on the catalyst surface over time the ideal triple phase environment for CO<sub>2</sub>RR is reduced, and the hydrophilic carbon surface was activated for hydrogen evolution (lower potential), thereby resulting in a shift of selectivity towards HER. The acid-base reaction results in the generation of HCO<sub>3</sub><sup>-</sup> and CO<sub>3</sub><sup>2-</sup>, which subsequently induce the degradation of UiO-66-NH<sub>2</sub> by displacing the linkers and coordinating with Zr atoms. This process leads to the formation of soluble [Zr<sub>2</sub>(OH)<sub>2</sub>(CO<sub>3</sub>)<sub>4</sub>]<sup>2-</sup>, BDC-NH<sub>2</sub><sup>2-</sup>, and CF<sub>3</sub>COO<sup>-</sup> accompanied by the production of small molecules, such as H<sub>2</sub>O and CO<sub>2</sub>, are generated.<sup>[28]</sup> On the other hand, the generated anions will facilitate the K<sup>+</sup> transport due to the electroneutrality in the photocathode, which will lead to salt precipitation. Therefore, aging of the MOF photocatalyst has to be considered, caused by flooding and salt precipitation. A more negative potential of -4.80 V was observed at ~2507 s without light illumination (Figure S8b). The large overpotential in this case is rather attributed to salt precipitation and inhibition of HER than to MOF degradation, as described above. This is in line with a reduced final production rate of HER compared to CO<sub>2</sub>RR for H23C2 in Figure S6a. In general, photocathodes configurations that lead to concentration of CO<sub>2</sub> and H<sub>2</sub>O in the double or triple phase boundaries within the CL seem to influence the selectivity of CO<sub>2</sub>RR towards alcohols, as shown in Figure 4a and S7a.

Under light irradiation, the photoexcited electrons in the MOF photocatalyst would further help to reduce H<sub>2</sub>O and CO<sub>2</sub> within a localized environment. Photoexcited electrons in the catalysts on CNF based photocathode participated in the CO<sub>2</sub>RR due to the buffering function of HCO<sub>3</sub><sup>-</sup> and lead to enhanced activity and selectivity towards CO<sub>2</sub>RR (Figure S6b and S7b). In addition, the water accumulated on the hydrophilic CNF surface facilitated the removal of deactivation compounds and salts, owing to the absence of ionomer in this electrode, resulting in an increased potential compared to the decreased potential marked in Figure S8a. However, as a result of fully wetted surface and OH<sup>-</sup>/HCO<sub>3</sub><sup>-</sup> accumulation, the UiO-66-NH<sub>2</sub> can degrade and finally become more inactive under visible light irradiation, resulting in a decline in catalytic performance.<sup>[28,33]</sup> The electrodes based on hydrophobic carbon layers have more positive final potential under light irradiation (Figure S8b), which can be attributed to improved dynamics of the electrochemical kinetics in the CO<sub>2</sub>RR. This also demonstrates that reduced energy consumption can be expected under visible light illumination with this configuration. However, the deactivation of MOFs catalysts leads to a decrease in light response and a higher overpotential with time. Finally, the additional MPL in the H23C2 carbon layer seems beneficial for controlling the local environment at the triple phase boundaries at the CL/MPL interface, resulting in a higher selectivity towards CO<sub>2</sub>RR (Figure S6b and S7b).

Energy-to-fuel conversion efficiency was subsequently calculated to assess the performance of the PEC system under light on the CO<sub>2</sub> reduction to fuels. Table 1 presents the energy-

**Table 1.** Energy-to-fuel (%) towards CO<sub>2</sub>RR with different photocathodes in PEC configuration under visible light irradiation (100 mW cm<sup>-2</sup>).

Carbon support layer	Energy-to-fuel (%)			
	HCOO <sup>-</sup>	CH <sub>3</sub> OH	C <sub>2</sub> H <sub>5</sub> OH	Total
H23	0.05	0.28	0.25	0.58
CNF	0.04	0.12	0.20	0.36
Toray H60	0.07	0.12	0.38	0.57
H23C2	0.44	0.39	0.23	1.06

to-fuel values reached for various photocathodes in the gas-phase photoelectrolyzer. The highest overall energy-to-fuel of 1.06% was achieved utilizing hydrophobic H23C2 based photocathodes, and selective formate production was with energy-to-fuel of 0.44%. The energy-to-fuel for formate of H23 and Toray H60 based photocathodes are comparable, suggesting that the catalysts are not selective to CO<sub>2</sub>RR. These results demonstrate that the CO<sub>2</sub> selectivity and activity of the reduction products can be tuned by the choice of carbon support layers and light irradiation.

The discussion presented above unequivocally establishes the significant influence of the carbon supports on mass transport, affecting products distribution, photocathode activity, and selectivity towards CO<sub>2</sub>RR. Despite the improved pore wetting and higher specific active interfacial area associated with hydrophilic CLs (Scheme 1 a and b), it is prone to flooding, leading to worse performance over time. Even if the CL is flooded over time or under high current density, the hydrophobic carbon layer is assumed to remain dry, enabling the catalysts at the CL/carbon layer interface to continue promoting CO<sub>2</sub>RR (Scheme 1c and 1d). It is essential to note that both degradation and salts precipitation require high concentrations of HCO<sub>3</sub><sup>-</sup> and CO<sub>3</sub><sup>2-</sup>, thus the competition of these two reactions further modulates the activity and selectivity of photocathodes. The photothermal conversion of photocathodes with different carbon layers also affect the product distribution by an increasing reaction temperature, especially with carbon nanofiber photocathodes, used in this work. Furthermore, the photoactive catalysts contribute to enhanced activity, while the deactivation of defective UiO-66-NH<sub>2</sub> results in deprotonated TFA modulator with -CF<sub>3</sub> groups, potentially further influencing the activity and selectivity towards CO<sub>2</sub>RR through its impact on pH, and the availability of H<sub>2</sub>O and CO<sub>2</sub> on the reaction sites.

## Conclusions

A zero-gap gas phase photoelectrolyzer for CO<sub>2</sub> reduction with a photocathode has been investigated, which has potential to improve product selectivity and energy utilization efficiency. For this purpose, a highly porous UiO-66-NH<sub>2</sub> catalyst with amine functionalization and unsaturated Zr sites has been engineered to achieve visible light absorption and enhanced CO<sub>2</sub> uptake. Different types of carbon layers were implemented as photocatalyst support in the photocathodes to tailor and

investigate the activity and selectivity towards CO<sub>2</sub>RR as function of the different local environment that resulted at the MOF photocatalyst. For the conversion of CO<sub>2</sub>, a superhydrophobic H23C2 based photocathode resulted in the best energy-to-fuel efficiency of 1.06% for hydrocarbons (formate, methanol and ethanol) on the UiO-66-NH<sub>2</sub> catalyst. This work clearly highlights the impact of porous carbon supports with different surface chemistry on the local reaction environment in the photocathode, which is determining the activity and product selectivity of CO<sub>2</sub> conversion towards hydrocarbon fuels. However, despite first insights and advancements with these types of systems, challenges with low activity and catalysts deactivation need to be overcome. Further studies on the gas phase conversion of CO<sub>2</sub> in PEC systems are recommended by using more active and chemically stable photocatalysts on superhydrophobic support layers, for enhancing the transport of reactants.

## Experimental Section

### Chemicals

Polyacrylonitrile (PAN, Mw = 150,000), zirconyl chloride octahydrate (ZrOCl<sub>2</sub>·8H<sub>2</sub>O), 2-Aminoterephthalic acid (H<sub>2</sub>BDC-NH<sub>2</sub>), trifluoroacetic acid (TFA), and N, N-Dimethylformamide (DMF) were purchased from Sigma-Aldrich and used as received. Nafion solution and isopropanol were used for the catalyst inks. Commercial UiO-66 was purchased from novoMOF and used as received. Commercial TorayH60 carbon paper and Freudenberg H23, H23C2 carbon fiber papers were used as carbon support layers. The different types of commercial and self-made carbon support layers used in this work are listed in Table 2. Freudenberg H23, Toray H60 and CNF are carbon fibers while Freudenberg H23C2 has an additional microporous carbon layer coated on one side of carbon fibers mat. All commercial carbon support layers were used without any pretreatment.

### Catalyst Preparation

2 mmol ZrOCl<sub>2</sub>·8H<sub>2</sub>O was dissolved in 25 mL of deionized water, and then 5 mL of TFA and 2 mmol H<sub>2</sub>BDC-NH<sub>2</sub> were added into the above solution. After ultrasonic treatment for 30 min, the solution was transferred to an autoclave for hydrothermal reaction at 100 °C for 12 hrs to obtain the UiO-66-NH<sub>2</sub> powder. For the synthesis of CNF@UiO-66-NH<sub>2</sub>, a CNF fiber mat with an area of 6.5 cm×3 cm and a thickness of about 180 μm was added into the hydrothermal solution, and the autoclave was put in an oven at 100 °C for 12 hrs. The resulting UiO-66-NH<sub>2</sub> powder and the UiO-66-NH<sub>2</sub>-CNF mats in the aqueous solution were washed with deionized water and ethanol several times to remove the remaining solvent. Finally, the samples with a pH of 6 were dried and activated in a vacuum oven at 150 °C for 8 hrs to obtain bulk powder (UiO-66-NH<sub>2</sub>) and CNF based photocathodes.

### Physico-Chemical Characterization

The microstructure of the UiO-66-NH<sub>2</sub> powder and UiO-66-NH<sub>2</sub>-CNF mats were investigated by scanning electron microscopy (SEM, Zeiss-Merlin). The atomic composition was evaluated using scanning electron microscopy with energy-dispersive X-ray spectroscopy (EDX). The X-ray diffraction (XRD) patterns were recorded on

**Table 2.** The properties of different carbon support layers employed in this work.

Carbon support layer	Material type	PTFE treatment	Microporous layer	Thickness ( $\mu\text{m}$ )	Wettability	Water contact angle (WCA) ( $^\circ$ )
H23	Carbon fiber paper	No	No	210	Superhydrophilic	–
CNF	Carbon nanofiber	No	No	180	Hydrophilic	$46.17 \pm 10.68$
Toray H60	Carbon fiber paper	Yes	No	190	Hydrophobic	$134.86 \pm 6.36$
H23C2	Carbon fiber paper	No	Yes	255	Hydrophobic (CFL side) Superhydrophobic (MPL side)	$129.34 \pm 2.70$ –

an Aeris powder diffractometer with Cu K-Alpha radiation ( $\lambda = 1.5608$ ) at 40 kV and 15 mA. The spectra measurements from 220–900 nm were performed to assess the adsorption capability using UV-vis spectrophotometry (UV-3600, Japan). Nitrogen adsorption-desorption curves were used to estimate the porosity and surface area by Micromeritics 3Flex at 77 K after pretreatment under a vacuum at 150 °C for 8 hrs. CO<sub>2</sub> adsorption curves were used to evaluate the CO<sub>2</sub> uptake by Micromeritics 3Flex at 298 K after pretreatment under a vacuum at 150 °C for 8 h. Thermogravimetric analysis (TGA) was applied to explore the content of UiO-66-NH<sub>2</sub> in hybrid nanofibers using NETZSCH STA 490PG with a heating rate of 5 °C min<sup>-1</sup> in the temperature range from room temperature to 800 °C in air. Fourier transform infrared spectroscopy (FTIR) was detected by Perkin Elmer Spectrum Two FTIR with 4 cm<sup>-1</sup> resolution and 8 scans in the range of 2000–400 cm<sup>-1</sup>. The contact angles of different carbon support layers were recorded with a drop-shape analyzer (Kruss DSA25, Germany). The volume of a water drop was 5  $\mu\text{L}$ .

### Photocathode Preparation

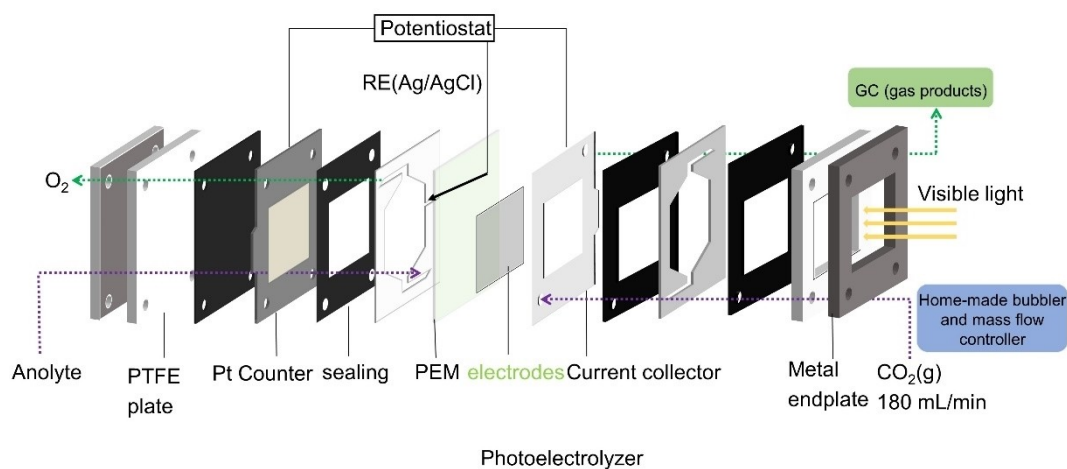
The photocathode preparation was carried out using hydrothermal method and a highly reproducible spray pyrolysis system based on automated deposition of catalytic inks<sup>[34]</sup> as listed in Table S1. These catalysts ink consisted of a combination of powder catalysts, Nafion@solution (5 wt%) as a binder and isopropanol as a solvent (97%), with a catalyst/Nafion mass ratio of 70/30. After ultrasonication for 30 min, the resulting homogenous inks were deposited onto different carbon support layers (3.5 × 4 cm<sup>2</sup>) via spray coating at 100 °C. The amount of catalyst loaded onto the

substrate was continuously weighed during deposition until reaching 1 mg cm<sup>-2</sup>, with a geometric area of 10 cm<sup>2</sup>. The free-standing CNF-based catalysts have been directly used as electrodes in photoelectrolyzer and assembled with Nafion@117 membrane and other cell components (i.e., gaskets and frames), as shown in Scheme 2.

### Photoelectrochemical Characterization

PEC characterization of the different photocathodes was carried out in an adapted PEC filter-press reactor (ElectroCell), which included a transparent plate (methacrylate sheet with a transparency index of 92%). The photocathode was illuminated with visible light ( $I_{\text{peak}}$  at 450 nm) provided by a LED lamp (Photolab LED 365-3/450-3, Apria Systems) with an intensity of 100 mW cm<sup>-2</sup>. Different photocathodes are utilized in gas-phase with CO<sub>2</sub> feed (180 mL min<sup>-1</sup>), whereas a platinized-titanium plate (ElectroCell) is used as the counter electrode as dark anode. A 0.5 M KHCO<sub>3</sub> (ACS reagent, Thermo Scientific) aqueous solution is employed as electrolyte in the anodic compartment, which is fed to the reactor at a rate per geometric surface area of 1 mL min<sup>-1</sup> cm<sup>-2</sup>. Both compartments are separated by a Nafion 117 cation exchange membrane (0.180 mm thick, >0.9 meq · g<sup>-1</sup> exchange capacity (Ion Power), which was coupled to the photocathode forming a MEA. A leak-free Ag/AgCl 3.4 M KCl electrode (ElectroCell) was used as a reference electrode placed in the anode compartment to ensure proper wetting.

First, each photocathode was subjected to on-off cyclic voltammetry (CV) measurements at a potential range of 0.5 V to –2.5 V to obtain the current density at a scan rate of 50 mV s<sup>-1</sup> using a potentiostat/galvanostat (AutoLab PGSTAT302N, Metrohm). The CV

**Scheme 2.** Schematic of zero-gas gas phase photoelectrolyzer in this work.

curves of all electrodes were analyzed for several scans, until a pseudo-stable behavior is observed. Then on-off chronopotentiometry analyses were carried out to study the voltage–time ( $V-t$ ) evolution for all photocathodes with a fixed current density of  $-7.5 \text{ mA cm}^{-2}$  applied to the photocathodes for 1 h.

### Zero-gap gas Phase Photoelectrolyzer for Continuous $\text{CO}_2$ Reduction

Scheme 2 displays the filter-press reactor elements employed for continuous single-pass PEC  $\text{CO}_2$ RR tests. The operation was carried out in the gas phase within the cathode compartment, where a humidified (home-made bubbler) pure  $\text{CO}_2$  stream at a rate of  $180 \text{ mL min}^{-1}$  was supplied to the photocathode, which forms a MEA with the ion exchange membrane that divides both compartments. The photocathode/dark anode configuration with an illuminated window of  $10 \text{ cm}^2$  comprises UiO-66- $\text{NH}_2$ -carbon layer or CNF@UiO-66- $\text{NH}_2$  as the photocathode and a Pt plate as a dark anode, where a thin lead-free Ag/AgCl reference electrode was located close to this anode to ensure its wettability. A  $0.5 \text{ M KHCO}_3$  solution was used as the anolyte at a flow rate of  $10 \text{ mL min}^{-1}$ . The  $\text{CO}_2$ RR process performance was assessed via applying a fixed current density of  $-7.5 \text{ mA cm}^{-2}$  for 1 h and the gas products were measured by Micro GC with a TCD detector at the reactor outlet (cathode side) every 4 min to calculate an averaged concentration of products obtained in each experiment, where the results that were two times lower/higher than the average value were discarded. Liquid products were also collected for further measurements. The concentration of alcohols in each sample was analyzed by duplicate in a headspace gas chromatograph (GCMS-QP2010 Ultra Shimadzu) equipped with a flame ionization detector (FID). An ion chromatography column (Dionex ICS 1100 using  $\text{Na}_2\text{CO}_3$  as eluent with a concentration of  $4.5 \text{ mM}$  and a flow rate of  $1 \text{ mL min}^{-1}$ ) was used to quantify the formate concentration obtained in the photocathode outlet throughout the experiment.

### Acknowledgements

We gratefully acknowledge core funding from Villum Fonden (Villum Experiment project Addlight, grant no. 40975) and financial support from Nordic Energy Research (CCU-NET project, grant no.100766). The authors also acknowledge the financial support of grant TED2021-129810B-C21 funded by MICIU/AEI/10.13039/501100011033/ and by the “European Union (NextGenerationEU/PRTR)” and by the COST action CA22147 “EU4MOF”.

### Conflict of Interests

The authors declare no conflict of interest.

**Keywords:** Zero-gap photoelectrolyzer ·  $\text{CO}_2$  conversion · Photocathodes · Mass transport · Metal organic frameworks (MOFs)

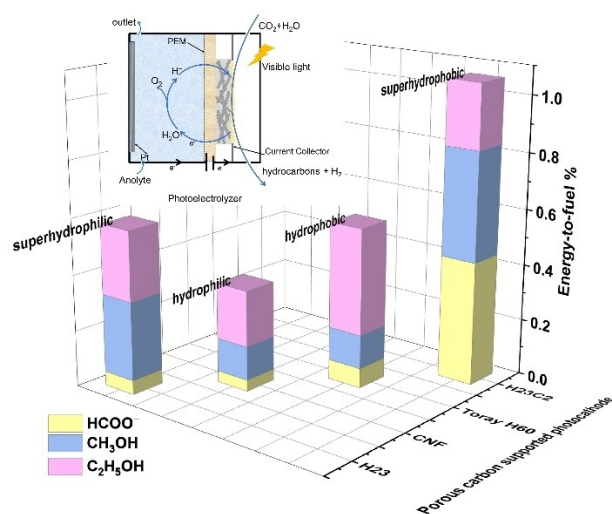
- [1] IEA, Paris <https://www.iea.org/reports/co2-emissions-in-2023> 2024, IEA, License: CC BY 4.0.  
[2] a) D. M. Weekes, D. A. Salvatore, A. Reyes, A. Huang, C. P. Berlinguette, *Acc. Chem. Res.* 2018, 51, 910–918; b) V. C. Hoang, T. S. Bui, H. T. D.

- Nguyen, T. T. Hoang, G. Rahman, Q. V. Le, D. L. T. Nguyen, *Environ. Res.* 2021, 202; c) Q. L. Wang, J. F. Liu, Q. Y. Li, J. J. Yang, *ChemSusChem* 2023, 16, e202202186.  
[3] T. Abbas, H. S. M. Yahya, N. A. S. Amin, *Energy Fuels* 2023, 37, 18330–18368.  
[4] C. Ampelli, F. Tavella, D. Giusi, A. M. Ronsisvalle, S. Perathoner, G. Centi, *Catal. Today* 2023, 421.  
[5] I. Merino-García, S. Castro, A. Irabien, I. Hernandez, V. Rodriguez, R. Camarillo, J. Rincon, J. Albo, *J. Environ. Chem. Eng.* 2022, 10.  
[6] W. Q. Shen, Z. P. Yang, J. J. Wang, J. W. Cui, Z. Y. Bao, D. B. Yu, M. N. Guo, G. Q. Xu, J. Lv, *ACS Sustainable Chem. Eng.* 2023, 11, 13451–13457.  
[7] a) H. Rabiee, L. Ge, J. Zhao, X. Q. Zhang, M. R. Li, S. H. Hu, S. Smart, T. E. Rufford, Z. H. Zhu, H. Wang, *Appl. Catal. B* 2022, 310; b) L. Xiong, X. B. Fu, Y. Zhou, P. Nian, Z. Wang, Q. Yue, *ACS Catal.* 2023, 13, 6652–6660; c) F. L. Yu, P. Leung, Q. Xu, S. Mavrikis, P. Nazarovs, A. K. Shah, L. Wang, C. P. de León, *J. Power Sources* 2023, 580.  
[8] a) K. Yang, R. Kas, W. A. Smith, T. Burdyny, *ACS Energy Lett.* 2020, 6, 33–40; b) M. D. Gálvez-Vázquez, P. Moreno-García, H. Xu, Y. H. Hou, H. F. Hu, I. Z. Montiel, A. V. Rudnev, S. Alinejad, V. Grozovski, B. J. Wiley, M. Arenz, P. Broekmann, *ACS Catal.* 2020, 10, 13096–13108.  
[9] R. Yanagi, T. Zhao, D. Solanki, Z. Pan, S. Hu, *ACS Energy Lett.* 2022, 7, 432–452.  
[10] J. Liu, C. Xia, S. Zaman, Y. Su, L. Tam, S. Chen, *J. Mater. Chem. A* 2022, 11, 16918–16932.  
[11] a) Z. M. Yang, D. Li, L. Xing, H. Xiang, J. Xuan, S. A. Cheng, E. H. Yu, A. D. Yang, *ACS Sustainable Chem. Eng.* 2021, 9, 351–361; b) A. M. Kalde, M. Grosseheide, S. Brosch, S. V. Pape, R. G. Keller, J. Linkhorst, M. Wessling, *Small* 2022, 18; c) S. Subramanian, K. Yang, M. Li, M. Sassenburg, M. Abdinejad, E. Irtem, J. Middelkoop, T. Burdyny, *ACS Energy Lett.* 2023, 8, 222–229.  
[12] L. C. Weng, A. T. Bell, A. Z. Weber, *Phys. Chem. Chem. Phys.* 2018, 20, 16973–16984.  
[13] a) P. Devi, R. Verma, J. P. Singh, *J. CO2 Util.* 2022, 65; b) W. J. Zhang, Z. Jin, Z. P. Chen, *Adv. Sci.* 2022, 9.  
[14] a) X. D. Kong, C. Wang, Z. F. Xu, Y. Z. Zhong, Y. Liu, L. Qin, J. Zeng, Z. G. Geng, *Nano Lett.* 2022, 22, 8000–8007; b) Y. C. Tan, K. B. Lee, H. Song, J. Oh, *Joule* 2020, 4, 1104–1120; c) C. Simon, D. Kartouzian, D. Müller, F. Wilhelm, H. A. Gasteiger, *J. Electrochem. Soc.* 2017, 164, F1697; d) D. L. T. Nguyen, C. W. Lee, J. Na, M.-C. Kim, N. D. K. Tu, S. Y. Lee, Y. J. Sa, D. H. Won, H.-S. Oh, H. Kim, B. K. Min, S. S. Han, U. Lee, Y. J. Hwang, *ACS Catal.* 2020, 10, 3222–3231; e) J. C. Douglin, J. A. Z. Zeledón, M. E. Kreider, R. K. Singh, M. B. Stevens, T. F. Jaramillo, D. R. Dekel, *Nat. Energy* 2023, 8, 1262–1272.  
[15] a) R. Senthil Kumar, S. Senthil Kumar, M. Anbu Kulandainathan, *Electrochem. Commun.* 2012, 25, 70–73; b) J. Albo, D. Vallejo, G. Beobide, O. Castillo, P. Castano, A. Irabien, *ChemSusChem* 2017, 10, 1100–1109; c) S. Mukhopadhyay, R. Shimoni, I. Liberman, R. Ifraemov, I. Rozenberg, I. Hod, *Angew. Chem.* 2021, 60, 13423–13429.  
[16] a) B. Shan, S. M. McIntyre, M. R. Armstrong, Y. Shen, B. Mu, *Ind. Eng. Chem. Res.* 2018, 57, 14233–14241; b) L. Liu, Z. Chen, J. Wang, D. Zhang, Y. Zhu, S. Ling, K. W. Huang, Y. Belmabkhout, K. Adil, Y. Zhang, B. Slater, M. Eddaoudi, Y. Han, *Nat. Chem.* 2019, 11, 622–628; c) N. C. Pham, T. K. Vo, Q. B. Nguyen, T. K. Nguyen, T. H. C. Nguyen, N. N. Dao, J. Kim, V. C. Nguyen, *Inorg. Chem. Commun.* 2023, 158, 111476.  
[17] a) A. F. Hernandez, R. K. Impastato, M. I. Hossain, B. D. Rabideau, T. G. Glover, *Langmuir* 2021, 37, 10439–10449; b) X. Wang, G. Yang, G. Chai, M. S. Nasir, S. Wang, X. Zheng, C. Wang, W. Yan, *Int. J. Hydrogen Energy* 2020, 45, 30634–30646.  
[18] a) Y. He, C. Li, X. B. Chen, Z. Shi, S. Feng, *ACS Appl. Mater. Interfaces* 2022, 14, 28977–28984; b) Y. L. Dong, H. R. Liu, S. M. Wang, G. W. Guan, Q. Y. Yang, *ACS Catal.* 2023, 23, 2547–2554.  
[19] W. W. Wang, S. J. Song, P. Wang, M. He, Z. Fang, X. L. Yuan, H. Li, C. Y. Li, X. Wang, Y. C. Wei, W. Y. Song, H. Xu, Z. X. Li, *ACS Catal.* 2023, 13, 4597–4610.  
[20] K. A. Adegoke, K. G. Akpomie, E. S. Okeke, C. Olisah, A. Malloum, N. W. Maxakato, J. O. Ighalo, J. Conradie, C. R. Ohoro, J. F. Amaku, K. O. Oyedotun, *Sep. Purif. Technol.* 2024, 331, 125456.  
[21] a) Z. Li, Z. Cao, C. Grande, W. Zhang, Y. Dou, X. Li, J. Fu, N. Shezad, F. Akhtar, A. Kaiser, *RSC Adv.* 2021, 12, 664–670; b) Y. Dou, W. Zhang, A. Kaiser, *Adv. Sci.* 2020, 7, 1902590.  
[22] a) Y. L. Wang, S. Zhang, Y. F. Zhao, J. Bedia, J. J. Rodriguez, C. Belver, *J. Environ. Chem. Eng.* 2021, 9, 106087; b) K. A. Kristoffersen, A. van Amerongen, U. Bocker, D. Lindberg, S. G. Wubshet, H. de Vogel-van den Bosch, S. J. Horn, N. K. Afseth, *Sci. Rep.* 2020, 10, 7844; c) Z.

- Zhai, X. Zhang, J. Wang, H. Li, Y. Sun, X. Hao, Y. Qin, B. Niu, C. Li, *Chem. Eng. J.* **2022**, *428*, 131720.
- [23] a) X. Fang, S. Wu, Y. Wu, W. Yang, Y. Li, J. He, P. Hong, M. Nie, C. Xie, Z. Wu, K. Zhang, L. Kong, J. Liu, *Appl. Surf. Sci.* **2020**, *518*, 146226; b) Y. Wang, L. Li, P. Dai, L. Yan, L. Cao, X. Gu, X. Zhao, *J. Mater. Chem. A* **2017**, *5*, 22372–22379; c) N. Zhang, D. Li, M. Mu, M. Lu, *Chem. Eng. J.* **2022**, *448*, 137467; d) M. R. Singh, Y. Kwon, Y. Lum, J. W. Ager 3rd, A. T. Bell, *J. Am. Chem. Soc.* **2016**, *138*, 13006–13012; e) J. Resasco, L. D. Chen, E. Clark, C. Tsai, C. Hahn, T. F. Jaramillo, K. Chan, A. T. Bell, *J. Am. Chem. Soc.* **2017**, *139*, 11277–11287.
- [24] a) Y. Fu, J. Wu, R. Du, K. Guo, R. Ma, F. Zhang, W. Zhu, M. Fan, *RSC Adv.* **2019**, *9*, 37733–37738; b) M. Athar, P. Rzepka, D. Thoeny, M. Ranocchiaro, J. Anton van Bokhoven, *RSC Adv.* **2021**, *11*, 38849–38855.
- [25] I. A. Lazaro, N. Almora-Barrios, S. Tatay, C. Popescu, C. Marti-Gastaldo, *Chem. Sci.* **2021**, *12*, 11839–11844.
- [26] a) X. J. Wang, G. R. Yang, G. D. Chai, M. S. Nasir, S. L. Wang, X. Zheng, C. Y. Wang, W. Yan, *Int. J. Hydrogen Energy* **2020**, *45*, 30634–30646; b) N. C. Yuan, Y. X. Mei, Y. W. Liu, Y. T. Xie, B. N. Lin, Y. H. Zhou, *J. CO<sub>2</sub> Util.* **2022**, *64*.
- [27] a) W. M. Zhang, J. Yan, Q. Su, J. Han, J. F. Gao, *J. Colloid Interface Sci.* **2022**, *612*, 66–75; b) J. Yan, W. Xiao, L. Chen, Z. Wu, J. Gao, H. Xue, *Desalination* **2021**, *516*, 115224.
- [28] J. Chu, F. S. Ke, Y. Wang, X. Feng, W. Chen, X. Ai, H. Yang, Y. Cao, *Commun. Chem.* **2020**, *3*, 5.
- [29] J. Park, Y.-j. Ko, C. Lim, H. Kim, B. K. Min, K.-Y. Lee, J. H. Koh, H.-S. Oh, W. H. Lee, *Chem. Eng. J.* **2023**, *453*, 139826.
- [30] a) M. Li, M. N. Idros, Y. Wu, T. Burdyny, S. Garg, X. S. Zhao, G. Wang, T. E. Rufford, *J. Mater. Chem. A* **2021**, *9*, 19369–19409; b) A. K. Buckley, M. Lee, T. Cheng, R. V. Kazantsev, D. M. Larson, W. A. Goddard III, F. D. Toste, F. M. Toma, *J. Am. Chem. Soc.* **2019**, *141*, 7355–7364.
- [31] L. Sun, J. Liu, Y. Zhao, J. Xu, Y. Li, *Carbon* **2019**, *145*, 352–358.
- [32] a) R. E. Vos, K. E. Kolmeijer, T. S. Jacobs, W. van der Stam, B. M. Weckhuysen, M. T. M. Koper, *ACS Catal.* **2023**, *13*, 8080–8091; b) S. Zong, A. Chen, M. Wiśniewski, L. Macheli, L. L. Jewell, D. Hildebrandt, X. Liu, *Carbon Capture Sci. Technol.* **2023**, *8*, 100133.
- [33] Y. Zhao, K. Zhao, J. Yin, J. Yang, J. Xu, Y. Gu, L. Liu, J. Luo, Y. Li, L. Sun, *J. Mater. Chem. A* **2019**, *7*, 24311–24319.
- [34] J. A. Abarca, G. Díaz-Sainz, I. Merino-García, G. Beobide, J. Albo, A. Irabien, *J. Environ. Chem. Eng.* **2023**, *11*, 109724.

---

Manuscript received: March 8, 2024  
Revised manuscript received: April 24, 2024  
Accepted manuscript online: April 30, 2024  
Version of record online: ■■■, ■■■



Porous carbon based photoanodes were utilized in investigating CO<sub>2</sub> reduction reactions within a zero-gap gas phase photoelectrolyzer. Various commercial carbon support layers with different wettability were

employed to modulate the local environment of cathodic reactions. The highest energy-to-fuel efficiency of 1.06% was achieved for hydrocarbons with H<sub>2</sub>3C<sub>2</sub> based photocathode under visible light illumination.

Dr. Y. Zhao, Dr. I. Merino-Garcia, Assoc. Prof. Dr. J. Albo, Assoc. Prof. Dr. A. Kaiser\*

1 – 10

**A Zero-Gap Gas Phase Photoelectrolyzer for CO<sub>2</sub> Reduction with Porous Carbon Supported Photocathodes**

